Colloids and Surfaces A: Physicochemical and Engineering Aspects 737 (2026) 139773

Contents lists available at ScienceDirect

Colloids and Surfaces A: Physicochemical and Engineering Aspects

journal homepage: www.elsevier.com/locate/colsurfa

Multifunctional green AuNPs towards a potential application in nanomedicine for tissue repair: In depth-XRPD and HPLC-MS/MS characterization

Michela Pinto [a], Gennaro Ventruti [b], Elena Andreucci [a], Anna Laurenzana [a], Vincenzo Piccolo [c], Giancarlo Capitani [d], Ritamaria Di Lorenzo [c], Maria Maisto [c], Teresa Di Serio [c], Sonia Laneri [c], Gian Carlo Tenore [c], Jennifer Gubitosa [e,f,*]

[a] Dipartimento di Scienze Biomediche Sperimentali e Cliniche "Mario Serio", Viale Morgagni 50, Florence 50134, Italy
[b] Department of Earth and Geoenvironmental Sciences, University of Bari Aldo Moro, Via E. Orabona 4, Bari 70125, Italy
[c] Department of Pharmacy, University of Naples Federico II, Via Domenico Montesano, 59, Naples 80131, Italy
[d] Dipartimento di Scienze dell'Ambiente e della Terra, Università degli Studi di Milano-Bicocca, Piazza della Scienza 4, Milano 20126, Italy
[e] University of Bari "Aldo Moro", Department of Chemistry, Via Orabona, 4, Bari 70126, Italy
[f] CNR NANOTEC – Institute of Nanotechnology –Bari Division c/o Department of Chemistry, University of Bari "Aldo Moro", Via Orabona, 4, Bari 70126, Italy

HIGHLIGHTS

- Up-cycling of Grape Pomace, a wine-making by-product, through synthesizing AuNPs.
- AuNPs' morphological, physicochemical characterization and assessment of the migratory potential via Franz diffusion cells.
- AuNPs functionalized by polyphenols from Grape Pomace for promoting tissue repair and modulating inflammation.

GRAPHICAL ABSTRACT

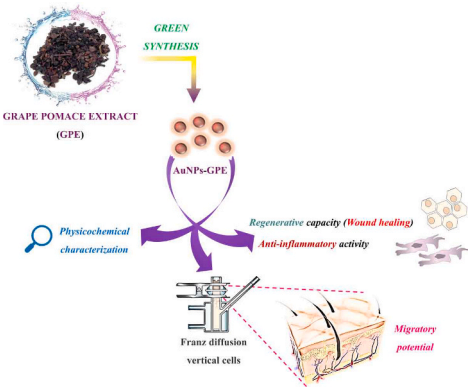

ARTICLE INFO

Keywords:
Gold nanoparticles
Grape pomace
Agrifood by-products valorization
Nanomedicine
Franz diffusion vertical cells
Wound healing
Inflammation

ABSTRACT

The primary aim of this study is to explore the use of green-synthesized gold nanoparticles, produced by reducing $HAuCl_4$ with a water-based polyphenolic extract derived from Grape Pomace, a winemaking by-product, for promoting tissue repair and modulating inflammation. A deepest study about their features has been performed by X-Ray Powder Diffraction analysis that provided a multiscale investigation into the nanocrystals' microstructure, revealing how the green synthesis conditions influence these features, strengthened by Transmission Electron Microscopy analyses' statements. Subsequently, a validated HPLC-MS/MS analysis identified the specific polyphenols that were retrieved on gold nanoparticles. Notably, polyphenols with glycosylation and higher

* Corresponding author at: University of Bari "Aldo Moro", Department of Chemistry, Via Orabona, 4, Bari 70126, Italy.
E-mail address: jennifer.gubitosa@uniba.it (J. Gubitosa).

https://doi.org/10.1016/j.colsurfa.2026.139773
Received 3 December 2025; Received in revised form 14 January 2026; Accepted 29 January 2026
Available online 31 January 2026

molecular weight, such as hyperoside and phloridzin, were retrieved to a minor extent, whereas aglycones like catechin, gallic acid, and quercetin were predominantly found on the nanoparticles' surfaces. Based on these findings, a preliminary evaluation of the transdermal permeation potential of the gold nanoparticles was achieved in porcine skin, as a model, using Franz diffusion cells. The results indicated that the nanoparticles themselves were not retained within the skin, suggesting minimal accumulation. Moreover, if polyphenols tightly bound to the gold nanoparticles, such as catechin and gallic acid, were released moderately, exhibiting limited transdermal permeation, in contrast, compounds weakly linked as chlorogenic acid, showed a significant release and thus higher permeation rates through skin. Importantly, beyond their physicochemical and transdermal characteristics, the synthesized gold nanoparticles demonstrated promising biological activities. They were found to promote angiogenesis in endothelial progenitor cells, supporting vascular formation, while simultaneously exerting anti-inflammatory effects on murine macrophages. This unique combination of pro-angiogenic and anti-inflammatory properties suggests their potential for application in regenerative medicine and vascular therapies.

1. Introduction

Since several years, nanoparticles are considered among the most important materials used across various fields. They exhibit high reactivity because of their extensive surface area, adjustable size, customizable surface properties for different uses, and shapes that can influence their physicochemical behavior [1]. Among nanomaterials, huge interest for gold nanoparticles (AuNPs) arose following the discovery of their remarkable properties, which made them preferable to others for biomedical applications. Indeed, gold offers several advantages, including ease of synthesis, tunable size and shape, excellent biocompatibility, low toxicity, and versatile surface functionalization [2]. Many advances have been thus obtained over the years, and the therapeutic potential of AuNPs extends across diverse biomedical applications. Among them, the anti-angiogenic and anti-inflammatory activities of AuNPs have emerged as promising strategies for treating diseases characterized by abnormal blood vessel formation and chronic inflammation, such as cancer and autoimmune disorders [3]. For example, traditionally synthesized AuNPs with well-defined structures have demonstrated significant activities. In retinal diseases, functionalized AuNPs can inhibit VEGF-induced endothelial cell proliferation and migration, offering a strategy to control pathological angiogenesis [4]. In models of ulcerative colitis, 5 nm AuNPs suppress pro-inflammatory cytokines such as IL-17, highlighting their anti-inflammatory effects in inflammatory bowel disease [5]. Similarly, in osteoarticular disorders such as osteoarthritis and rheumatoid arthritis, AuNPs display both anti-inflammatory and osteogenic activities, contributing to reduced inflammation and improved bone health [6]. Another study demonstrates that CO-rich AuNPs, synthesized via pulsed laser-driven CO_2 reduction, can enhance endothelial cell migration and angiogenesis more effectively than conventional CO-releasing molecules, while also promoting histone acetylation [7]. However, a new era for noble metals-based nanomaterials' synthesis seems to be projected in embracing Green Chemistry principles, as emerges from literature, particularly if referring to the green synthesis of AuNPs [8–12]. Fruits, plants, fungi, and so on, have been widely used over the years as raw natural matrices from which bioactive molecules can be extracted to both synthesize and functionalize AuNPs [13]. Indeed, plant-mediated gold nanoparticles have been widely explored for biological applications, particularly for anti-inflammatory or wound-healing purposes; however, most studies rely on complex and poorly defined phytochemical surface coatings, limiting structure–function correlations [14–17]. For instance, AuNPs synthesized from Capsicum extracts demonstrate antioxidant, anti-angiogenic, and anti-inflammatory effects [3]. Similarly, green-synthesized AuNPs conjugated with bioactive compounds such as liquiritin and isoliquiritin apioside reduce nitric oxide production in macrophages, highlighting their anti-inflammatory potential [18]. These approaches provide not only sustainable synthesis routes but also nanoparticles with bio-functional surfaces that improve cellular interactions. Mechanistically, the biological effects of AuNPs are mediated through multiple pathways. Their activity is size-dependent, with smaller nanoparticles often inducing pro-inflammatory responses, while larger particles may suppress inflammation via macrophage polarization. Additionally, AuNPs can modulate signaling pathways such as NF-κB, MAPK, and PI3K/Akt, leading to reduced expression of pro-inflammatory cytokines and inhibition of pathological angiogenesis [5]. Despite these advances, most studies report either anti-inflammatory or anti-angiogenic effects in isolation. So, it remains a lack of AuNPs that simultaneously promote angiogenesis and modulate inflammation, a combination crucial for regenerative medicine applications. At the same time, the use of green synthesized AuNPs is not well documented for these purposes. Not surprisingly, green-synthesized AuNPs exhibit superior biocompatibility and unique physicochemical properties, largely related to the ability of functionalizing their surfaces with bioactive molecules, which in turn could enhance their therapeutic potential [11,12]. Moreover, in this scenario, an emerging trend is focusing on the use of agrifood wastes and by-products for enabling AuNPs' synthesis according to Circular Economy. Thus, wastes and by-products were valorizing as precious resources through upcycling, instead of their improper disposal, ensuring more rational management [11,12]. This approach not only reduces waste but also aligns with the goals of the European Green Deal by minimizing environmental pollution, a critical challenge today, while producing nanoparticles for broad biomedical applications [11,12]. For these reasons, the present work proposes the application, in nanomedicine, of AuNPs synthesized by Gubitosa *et al.* [11] from Grape Pomace (Figure S1 **A**), a well-known winemaking by-product typical of the Apulia region, selected for its extremely high content of polyphenols [19]. Specifically, a water-based polyphenolic extract was obtained, named Grape Pomace Extract (GPE) (Figure S1 **B**), acting as reductant agent for synthesizing gold nanoparticles (from now named AuNPs-GPE). AuNPs-GPE occurred thus functionalized with polyphenols, 36 of which have already been analytically identified by authors [19]. On the other hand, Gubitosa *et al.* [11] showed yet that these AuNPs-GPE had high thermal stability in the temperature range between 10 and 80°C. A certain instability at pH 2 was noted, resulting in a massive AuNPs-GPE aggregation. Ionic strength negatively affected the AuNPs-GPE stability if increasing concentration and valence of the examined ionic species, due to the charge screening [11]. Furthermore, AuNPs-GPE exhibited, thanks to the phenolic functionalization, antioxidant features, and inhibited tyrosinase enzyme responsible for melanogenesis in vivo, resulting in a skin lightening effect. The reported *in-vitro* investigation of AuNPs-GPE antioxidant activity, performed on normal human dermal fibroblasts, revealed their cytoprotective effects against ROS-induced cellular DNA damage [11]. Differently, this paper integrates the surface chemical and physical features of AuNPs-GPE with biologically relevant assays, demonstrating their potential for tissue repair, vascular regeneration, and inflammation modulation. AuNPs-GPE migratory potential through porcine skin using Franz diffusion cells was also assessed for investigating both nanoparticles and polyphenols migration across a biological barrier, addressing an aspect that is critical for interfacial and translational applications but rarely considered in green-synthesized AuNPs.

Together, these results highlight how sustainable synthesis and surface chemistry control the structural and interfacial behavior of AuNPs. Indeed, it is worth mentioning that the surface functionalization also could affect how AuNPs penetrate the skin, a critical factor for topical and transdermal applications [20]. Therefore, for pursuing the aforementioned goals, a validated HPLC-MS/MS method was applied for the simultaneous quantification of twenty polyphenols retrieved in the AuNPs-GPE sample, enabling direct correlation between AuNPs' surface chemistry and biological response. Compared to conventional LC-based approaches, the method showed high sensitivity and reproducibility, ensuring reliable analysis even in complex colloidal matrices. In parallel, special emphasis has been also placed on X-Ray Powder Diffraction (XRPD) analysis, which plays a central role in revealing additional features. Beyond simply verifying the formation of gold's face-centered cubic structure, the XRPD data enabled a detailed, multiscale investigation of the nanocrystals' microstructure, providing key insights into sample purity, crystallite size, and the presence of structural defects [21]. An advanced X-ray line profile analysis using convolutional whole profile fitting [22] was applied to explore these microstructural features, demonstrating how synthesis conditions affect nanoparticle quality. Unlike traditional methods that focus on individual peak widths, Whole Powder Pattern Modelling (WPPM) fitted the entire diffraction pattern and simultaneously accounted for size distributions, anisotropic strain, lattice defects, and instrumental factors through physically grounded models of microstructure. WPPM makes it possible to extract detailed quantitative data on size and defect distributions by optimizing microstructural parameters to best match the observed data. This approach offers a comprehensive characterization of crystallite size distributions, strain fields, defect densities, and even stacking faults or dislocations. Applied to gold nanocrystals, WPPM can reveal subtle microstructural details inaccessible to simpler methods, offering a richer and more accurate picture of their structure; information useful for understanding and predicting the AuNPs-GPE behavior in biological microenvironments.

The assessment of AuNPs-GPE migratory potential through skin was performed using Franz diffusion cells, also known as vertical diffusion cells. These devices mimic the skin barrier under controlled conditions, allowing precise measurement of nanoparticles' permeation and retention over time. Franz cells enable the evaluation of the influence of different functionalization on the passage of AuNPs through the various skin layers. Such studies are critical to understanding AuNPs behavior in physiological environments and addressing potential health risks. Moreover, when these studies are combined with porcine skin, a validated surrogate for human tissue, they provide reproducible and physiologically relevant data. Indeed, this model has been widely applied to AuNPs, showing that particle size and skin integrity markedly affect permeation [23,24]. More recently, functionalized AuNPs have been tested in Franz cells, confirming their usefulness for studying how nanoparticle surface chemistry influences transdermal delivery [20]. This provides essential data prior to clinical applications. Furthermore, in this work, Franz cells were employed to evaluate the possible release of polyphenols from AuNPs-GPE, assessing their migratory potential across the skin barrier, and investigating their fate. Simultaneously, it was demonstrated that AuNPs-GPE uniquely combined pro-angiogenic activity in endothelial progenitor cells with anti-inflammatory effects in macrophages. The first outcome from *in-vitro* test was further outlined regarding their potential features to behave as promoters of cellular migration and tissue repair, but at the same time, indicating the necessity for careful dose optimization to avoid cytotoxic effects.

2. Experimental

2.1. Extraction of the polyphenolic fraction from grape pomace

Primitivo's Grape Pomace, a mixture of grape seeds, skin, and stems (Figure S1 **A**), was subjected to a fermentation process for 20 days at a temperature of 27 ± 2 °C, before being supplied by "L'Archetipo", a winemaking farm, Contrada Tafuri sp21, km7, Castellaneta, Taranto/Puglia 74011 (Italy), and stored at −19°C as soon as received. For extracting polyphenols, 2 g of grape pomace were introduced into a beaker containing 50 mL of deionized water that was boiled for 5 min. The obtained GPE, exhibiting a light pink color (Figure S1 **B**), was separated from the solid spent residue after centrifuging at 6000 rpm for 20 min with the help of a Thermo Scientific Heraeus Multifuge X3R Centrifuge, filtered and stored at −19°C before its use [11].

2.2. Green AuNPs-GPE synthetic protocol

The protocol proposed by Gubitosa *et al*[11]. was used and herein summarized. A stock solution of $HAuCl_4$ (Sigma-Aldrich, Milan, Italy) 1×10^{-3} M was prepared in deionized water. As second step, 250 µL of this solution were mixed with 1.750 mL of GPE to reach a final $HAuCl_4$ concentration of 1.25×10^{-4} M in the reaction batch having a total volume of 2 mL. The resulting solution was kept under moderate stirring for 24 h before obtaining the AuNPs-GPE colloidal dispersion by centrifuging twice at 8000 rpm for 20 min using a D2012 High Speed Mini Centrifuge (Scheme 1). A molar absorption coefficient of 3.36×10^{9} $M^{-1}cm^{-1}$ was adopted to infer the AuNPs-GPE stock colloidal solution concentration through UV-Visible spectroscopy, by applying the Lambert-Beer law. A mean AuNPs-GPE concentration of 1×10^{-11} M was calculated, corresponding to 1 mg/mL of AuNPs (1.79×10^{11} nanoparticles/mL) [11].

2.3. UV-Visible spectroscopy

A Varian CARY 5 UV-Vis-NIR spectrophotometer (Varian Inc., now Agilent Technologies Inc., Santa Clara, CA, USA) was used to collect AuNPs absorption spectra in the range 200–800 nm, at a 1 nm/s scan rate, employing a quartz cuvette having 1 cm path length.

2.4. Transmission electron microscopy (TEM)

Transmission electron microscopy (TEM) observations were performed at the Platform of Microscopy of the University of Milano-Bicocca with a JEOL JEM 2100 P instrument, equipped with a LaB_6 source and operated at 200 kV. The as receive suspension of gold nanoparticles (AuNPs-GPE) was shaken and ultrasonicated, then about 10 µL of suspension was pipetted on a C-coated, 300-mesh Cu-grid. Bright field (BF) images and selected area diffraction (SAED) patterns were acquired with a 3k x 3k Gatan Rio CMOS camera. The particles analysis was performed with Digital Micrograph v. 3.32 (Gatan), paying attention to eliminating from the statistics all touching particles.

2.5. Dynamic light scattering (DLS) and Zeta potential measurements

The AuNPs-GPE hydrodynamic diameter and surface charge were investigated by laser doppler velocimetry using a Zetasizer Nano ZS (Malvern Instruments Ltd., Worcestershire, UK). Experiments were performed in triplicate, and the mean values and standard deviations were calculated directly by the software.

2.6. X-ray powder diffraction (XRPD)

X-ray powder diffraction (XRPD) data were collected using an Empyrean PANalytical diffractometer equipped with a 1.8 kW CuKα ceramic X-ray tube (λ_{avg} = 1.5418 Å) and a real-time multiple strip (RTMS) PIXcel3D detector. The sample was prepared by carefully applying droplets of the solution onto a zero-background holder (ZBH) made from single-crystal silicon, cut at a specific orientation parallel to the Si (510) plane, and allowing it to dry at room temperature. Analytical conditions were: 40 mA and 40 kV, a scanning speed of 0.026°/s, and a 2θ range from 30° to 120°. The system included a set of

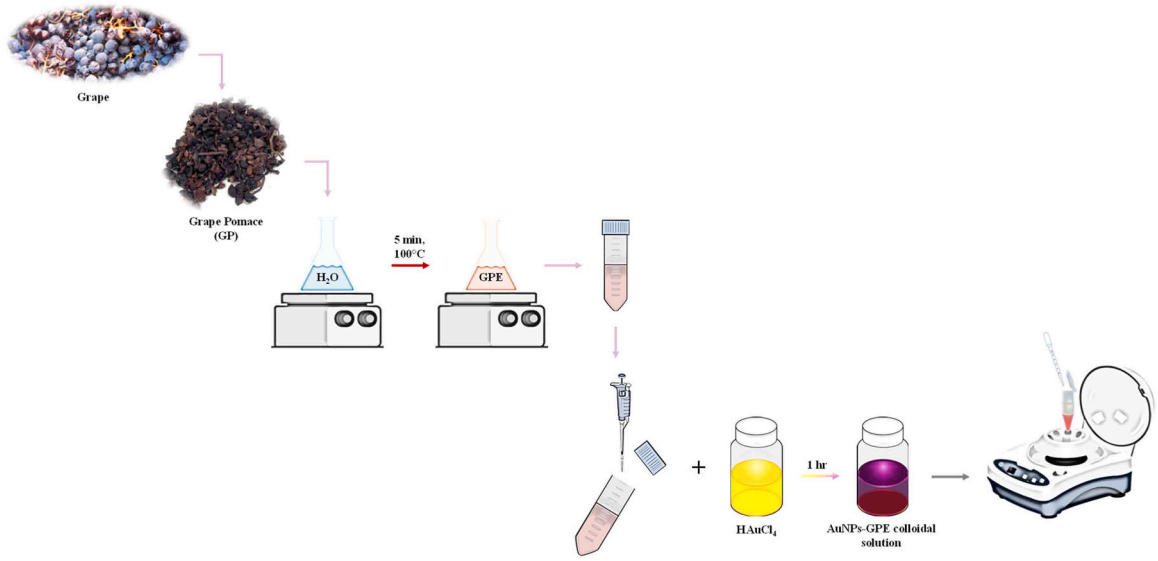

Scheme 1. All the steps followed for synthesizing AuNPs-GPE through a Green protocol.

narrow slits: a 0.0625° divergence slit, a 0.125° antiscatter slit, and 0.02 rad Soller slits. Multiple scans were combined to improve the signal-to-noise ratio. Preliminary structural analysis of the formed AuNPs, including determination of lattice parameters and sample purity checks, was performed using the BGMN software [21]. To extract microstructural parameters such as average crystallite size and distribution, as well as line and planar defect concentrations, Whole Powder Pattern Modelling (WPPM) fitting was applied using the PMK2 program [26,27]. In this procedure, all peak profiles are simultaneously fitted by convolving contributions from the instrument, grain-size distribution, and distortion profiles across the entire measured 2θ range. The instrumental contribution was obtained by parameterizing the profiles of a line profile standard with negligible broadening (in the present case LaB_6, NIST SRM660a). Background was modeled using a Chebyshev polynomial. Lattice constants, zero error, and sample displacement were also included as input parameters. The fitting process used the nonlinear Marquardt-Levenberg least-squares algorithm to minimize the Weighted Sum of Squared Residuals (WSSR), optimizing the physical parameters that describe the microstructural features.

2.7. AuNPs-GPE migratory potential investigation through porcine skin via Franz vertical diffusion cells: Ex Vivo Tests

2.7.1. Tissue preparation

Skin samples were provided by a local slaughterhouse (Se.ma. Sepe s. r.l., Avellino, Italy). All experiments were conducted on fresh porcine skin within 24 h *postmortem*, with samples stored at 4 °C until use. Before experimentation, the skin was carefully prepared by removing hair and subcutaneous fat. The tissue was then placed on filter paper (Fisherbrand™ Grade 601, Fisher Scientific, Leicestershire, UK) and cut into uniform sections measuring 2 cm^2 for subsequent assembly in Franz diffusion cells. The integrity of the porcine skin was assessed by measuring its impedance, ensuring that both the epidermal and dermal layers were included, as previously described [28,29].

2.7.2. Experimental setup

Porcine skin explants were mounted onto the receptor compartments of Franz vertical diffusion cells (Ø 9 mm; SES GmbH-Analyse System, Bechenheim, Germany), featuring an effective diffusion area of 0.6 cm^2 and a receptor volume of 5 mL [30]. Full-thickness skin samples were rinsed three times with 1 mL of distilled water before mounting. Each explant was carefully positioned between the two halves of the diffusion cell, ensuring the stratum corneum faced the donor compartment.

The receptor compartment was filled with 5 mL of phosphate-buffered saline (PBS, 0.1 M, pH 7.4), while the donor compartment received 500 μL of a solution containing AuNPs-GPE. A specialized cap was placed on the donor compartment to ensure a constant internal pressure of 1 atm.

Franz cells were maintained at 37 °C in a thermostatic water bath (Enzymatic Digester GDE, 230 V/50–60 Hz, VELP Scientifica, Usmate Velate, Italy) placed on a MultiStirrer (VELP Scientifica, Usmate Velate, Italy) and a magnetic stir bar was placed into the receptor compartment to provide continuous stirring throughout the experiment.

Aliquots were collected from both donor and receptor compartments at each designated exposure time (4, 8, and 24 h). Then, skin membranes were taken from the diffusion cells and gently wiped three times with tissue soaked in distilled water to remove residual AuNPs-GPE. Subsequently, the skin was sectioned according to the permeation area (0.6 cm^2) and epidermal separation from the dermis was performed by gentle scraping with tweezers (Semken-Taylor Rette No. 1, 12.5 cm, Asa Dental Spa) followed by surgical dissector (Pikdare Spa, Casnate con Bernate, Como, Italy) [31,32] after drying up to 50 °C through an air dryer for 30 s. All experiments were conducted in triplicate. The samples were freeze-dried and extracted with 1,5 mL of a 80 % methanolic solution with 1 % of formic acid, sonicated for 20 min, and shaked at 600 rpm for 20 min at room temperature. After the extraction time, skin samples were discharged, and the extraction solvent was transferred to plastic vials and then centrifuged at 12000 rpm for 10 min. The supernatant was filtered using nylon syringe filters 0.22 μm (Phenomenex, Bologna, Italy) and evaporated to dryness under a light stream of nitrogen. The dried extracts were reconstituted in methanol at a concentration of 10 mg/mL and stored at −20 °C until analysis.

2.7.3. HPLC-MS analysis of franz's diffusion cell system

An HPLC Agilent 1200 coupled with an Agilent Technologies 6470-triple quadrupole mass spectrometer (Agilent Technologies, Palo Alto, CA, USA) was used for the analysis. Elution was performed on a ACQUITY UPLC BEH C18 column (50 mm × 2.1 mm, 1.7 μm; Waters®, Milford, MA, USA). The mobile phases were water with 0.1 % formic acid (A) and acetonitrile with 0.1 % formic acid (B). The elution gradient was performed according to the following conditions: 0–4 min, isocratic on 2 % phase B; 4–30 min, linear gradient from 2 % to 30 % B; 30–32 min, linear gradient from 30 % to 95 % B; 32–37 min, isocratic on 95 % B; 37–41 min, isocratic on 2 % B for column recondition. The column temperature was set at 50 °C, inject volume was 5 μL, and the flow rate was set at 0.50 mL/min. The source was a heated electrospray

interface (HESI) operated in negative ionization with multiple reaction monitoring (MRM) scanning modes. One MRM transition was used as a quantifier transition and a second MRM transition served as a qualifier transition. MRM transitions, collision energy (eV) and fragmentor values of each polyphenol were summarized in Table S1. Argon was used as a gas for collision-induced fragmentation. The MRM analyte parameters were optimized using a methanolic solution of each polyphenol at a concentration of 10 ppm. Compounds were quantified according to a calibration curve ($R^2 \geq 0.99$) made with triplicate injections at each concentration. The ion source was set using the following parameters: gas temperature: 300 °C; gas flow rate: 7 L/min; gas temperature: 320 °C; sheath gas flow rate: 11 L/min; capillary voltage: 2500 V; nebulizer pressure: 45 psi; and nozzle voltage: 2000 V.

The Occurrence degree % of each polyphenol on the AuNPs-GPE surface was calculated by comparing the quantitative MRM peak areas obtained for GPE and for the supernatant recovered after AuNPs-GPE synthesis and centrifugation steps. In detail, it was determined by the difference between the analyte area in the GPE and that remaining in the supernatant, and determined through the following equation:

$$Occurrence\ degree \quad (\%) \quad = (Area_{GPE} - Area_{Supernatant}) / Area_{GPE} \quad * 100$$

2.7.4. Analytical validation of the HPLC-MS/MS method

As recommended by the ICH guidelines, to validate an analytical method, linearity, sensitivity, analytical stability and the carry-over were evaluated. An analytical standard of each polyphenol was used to develop and validate the HPLC-MS/MS method. A stock solution of each compound was prepared at a concentration of 50 ppm using an 80 % methanolic solution. Individual stock solutions were diluted to prepare a standard mixture solution of each standard at a concentration of 5 ppm in an 80 % methanolic solution. The calibration curves ($R^2 \geq 0.99$) were obtained by diluting the standards mixture in 80 % methanolic solution with a dilution factor of 2. The standard mixture dilutions were analyzed in triplicate injections at each concentration. The calibration lines were constructed by plotting the peak area against the standard concentration to evaluate the linearity of the standard response. Limit of detection (LOD) and limit of quantification (LOQ) were determined to evaluate the sensitivity of the method. The LOD and LOQ were determined using the signal-to-noise (S/N) ratio, as calculated directly by the instrument software (Agilent MassHunter). The LOD was defined as the lowest concentration with an S/N ratio of 3:1, the LOQ was defined as the lowest concentration with an S/N ratio of 10:1. To monitor analytical stability throughout the HPLC-MS/MS sequence, quality control (QC) samples were prepared using a mixed standard solution of polyphenols at a concentration of 5 ppm. QC samples were injected at regular intervals (every 8–10 analytical samples) across the sequence. For each QC injection, peak area and retention time were recorded. Analytical performance was considered acceptable if the relative standard deviation (RSD%) of the peak area for each polyphenol did not exceed 5 %, and if retention time variation remained within ± 0.2 min. To assess the potential carry-over in the HPLC-MS/MS system, a sequence of three injections of a high-concentration standard solution of each polyphenol at a concentration of 5 ppm was followed by three injections of a low-concentration solution, corresponding to the lowest calibration point of the respective standard curve for each compound. The carry-over effect was calculated as follows:

Carry-over (%) = L1-mean(L2,L3)/ H3-mean(L2,L3)*100

where L1 is the first injection of low concentration solution, L2 is the second injection of low concentration solution, L3 is the third injection of low concentration solution, and H3 is the third injection of high concentration solution.

2.8. In vitro viability, wound healing, and Capillary morphogenic assays

2.8.1. MTT cell viability assay

5×10^3/well cells were plated in a 96-well plate, after overnight pretreatment with AuNPs. 24 h later, cells were incubated for 2 h at 37 °C in the dark with 0.5 mg/mL 3-(4,5-dimethylthiazol-2-yl)-2,5-diphenyl tetrazolium bromide (MTT) in medium without phenol red. MTT was removed, and cells were lysed in 100 µl DMSO. Absorbance was recorded at 595 nm with Multiskan FC multiplate reader (Thermofisher, Italy).

2.8.2. RT e qPCR

Total RNA was prepared using Tri Reagent (Merk Life Sciences S.r.l., Milan, Italy) and quantified with the NanoDrop™ 8000 Spectrophotometer (Thermo Fisher Scientific, Milan, Italy). Reverse transcription was performed with the Prime ScriptTM FAST RT reagent Kit with gDNA Eraser (Takara) according to the manufacturer's instructions. Selected genes were evaluated at the Bio-Rad CFX96 Touch™ Real-Time PCR Detection System (Bio-Rad, Milan, Italy) using SsoAdvanced Universal SYBR Green Supermix (Bio-Rad, Milan, Italy). The murine primer sequences are the following: IL-1β FW: TGG ACC TTC CAG GAT GAG GAC A; IL-1β RV: GTT CAT CTC GGA GCC TGT AGT G; TNF-α FW: GGT GCC TAT GTC TCA GCC TCT T; TNF-α RV: GCC ATA GAA CTG ATG AGA GGG AG; 18S FW: CGC CGC TAG AGG TGA AAT TCT; 18S RV: CGA ACC TCC GAC TTT CGT TCT.

2.8.3. In Vitro wound healing assay

2.5×10^5 cells were seeded in 6-well plates and treated overnight with AuNPs. Cells were then detached using Accutase and resuspended at a density of 2.5×10^5 cells in 400 µL of medium. A total volume of 100 µL cell suspension was plated into each well of a Culture-Insert 4 Well (Ibidi). After 4–6 h of incubation to allow cell adhesion, the inserts were carefully removed to generate a defined cell-free gap. Phase-contrast images were acquired using an EVOS M5000 optical microscope (Thermo Fisher Scientific) at 0 h and 24 h after insert removal. The images obtained were subsequently analyzed to determine the wound closure rate using the MRI Wound Healing Tool in ImageJ.

2.8.4. Capillary morphogenic assay

A total of 0.2×10^5 ECFCs/well were plated on 96-well plates precoated with 50 µl Matrigel (Corning) and cultured in FBS-free EBM-2 medium. Cells were incubated for 6 h at 37°C and pictures were acquired using an EVOS M5000 optical microscope (Thermo Fisher Scientific). The angiogenesis analyzer tool of ImageJ software, by measuring the number of nodes, segments, meshes and junctions per field, provided the statistical analysis for each experimental condition tested.

2.8.5. Immunofluorescence

RAW 264.7 cells (5×10^4) were seeded in Ibidi µ-Slide 8-well chambers and treated with 1 µg/mL LPS (Sigma Aldrich) for 1 h, followed by a medium change and treatment with AuNPs for 5 h. Subsequently, the cells were fixed with 3.7 % paraformaldehyde for 20 min at 4 °C and permeabilized with 0.1 % Triton X-100 in PBS for 10 min at room temperature. Cells were then incubated with blocking buffer (0.1 % Triton X-100 in PBS) for 1 h. Subsequently, the samples were stained with anti-NF-κB p65 primary antibody overnight at 4 °C in the dark, followed by incubation with Alexa Fluor 647-conjugated anti-rabbit secondary antibody (Thermo Fisher Scientific) at room temperature in the dark. Finally, nuclei were counterstained with DAPI for 20 min at room temperature in the dark. Images were acquired using a SP8 Leica confocal microscope. The immunofluorescence signal was quantified using JACOP tool of ImageJ software.

2.8.6. Statistical analysis

Statistical analysis was performed with GraphPad Prism 6 software

by *t*-test, one-way analysis of variance (ANOVA), and two-way ANOVA. Values are presented as mean ± standard deviation (SD).

3. Results and discussion

3.1. Functionalized green AuNPs-GPE: synthesis, morphological, physical and chemical characterization. A brief overview

Since natural matrices are plentiful of bioactive molecules exhibiting antioxidant properties, an approach for synthesizing AuNPs has been followed according to Green Chemistry and Circular Economy principles, as an alternative to the conventional methods well known in literature [9–12,33,34].

For the purpose, an appropriate amount of GPE was mixed with a $HAuCl_4$ solution having a concentration of 10^{-3} M. Thus, green and functionalized AuNPs- GPE were rapidly obtained in one hour, observing the color changes from light yellow to violet, and characterized through UV–VIS [35], TEM, DLS, and Zeta potential techniques. Interestingly, the TEM observations **(**Fig. 1 **A-C**, and **S2 A-D)** aligned with the XRPD outcomes, revealed AuNPs with dimensions of a few tens of a nanometer (average equal area circle diameter 17 ± 4 nm). Particles were mostly globular, although some elongated particles and rods were also observed, as well as larger, flat, polygonal particles (Figure S2A). The nature of the latter could not be disclosed, but most probably it is not about Au. At higher magnification (Fig. 1), in BF images, AuNPs-GPE showed a quite large density of defects, especially planar defects such as twinning, which make the actual coherently scattering domains much smaller than the particles themselves. Therefore, if the average particle size diameter measured on TEM images was around 17 nm, the actual single crystal domain may be as small as a few nm. Finally, very small, 1–2 nm wide, round particles were observed at high magnification (Fig. 1). Also in this case, their nature could not be disclosed. On the other hand, DLS measurements performed at pH 6, r.t., restituted a hydrodynamic diameter of 30 ± 5 nm, and a negative surface charge (-40 mV ± 2 mV). Moreover, the UV-Visible spectrum of AuNPs-GPE colloidal solution showed a characteristic surface plasmon resonance (SPR) band set at 550 nm, indicative of the colloidal gold presence in solution Fig. 1 **(D)**.

3.2. X-ray powder diffraction (XRPD)

More details were inferred by XRPD technique. The cell parameter, refined, with the LeBail method in the Fm- 3 m space group using the BGMN software [25] was equal to 4.077(2) Å. All peaks (Fig. 1**E**) could be attributed to the typical planes for a face-centered cubic (FCC) structure, namely (111), (200), (220), (311) and (222), (400), (331) and (420). SAED patterns confirmed the crystalline nature of the particles and the cubic FCC Au structure (Figure S2 **B, C**). No other reflections were detected in the diffractogram, suggesting that the synthesized sample is apparently without impurities within the detection limit. Significant peak broadening (from 1.5° to 2.5° in the whole 2Θ range) exceeding the instrumental contribution (about 0.07° 2θ) was observed suggesting crystallite smallness and enhancement of lattice strain due to dislocations and planar defects. Integral breadth (IB) methods [36] are often used to quickly estimate the "size-strain" effect in materials. The Scherrer formula [37] and the Williamson-Hall plot [38], along with later modifications [39] are useful for a basic, mostly qualitative look at how domain size and strain affect IB.

From the Scherrer plot the estimated apparent diameter of the crystallite, D, was found to be around 9.67 nm, assuming a spherical shape, based on the relation $\langle t \rangle_{vol} = ¾\ D$ [40,41]. The Scherrer plot revealed a relatively low R-squared value of approximately 0.71, indicating that strain influences are affecting the sample (Figure S3).

Figure S4 shows the WH plot for the investigated sample. The results obtained suggest that lattice deformations vary across different crystalline planes, since likely the anisotropic nature of the dislocation strain field, elastic properties [42], and effects from planar defects.

It's also important to note that the presence of a size distribution—especially a lognormal one—is incompatible with the assumptions behind the WH method and, more broadly, with integral breadth methods used for separating size and strain effects. To overcome these limitations (e.g.: anisotropism, dislocations, planar defects, size and shape distribution), an innovative technique, the Whole Powder Pattern Modelling (WPPM), has been used. According to this approach, line profiles can be described directly in terms of physical models of the microstructure and lattice defects present in the studied material, avoiding using arbitrary (a priori selected) profile functions, whose parameters are not directly and univocally related to physically observable quantities.

Under the WPPM formalism a generic peak in the experimental pattern is modelled by a line profile, *Ig*, resulting from the convolution of instrumental factors, grain-size distribution and crystal lattice defects (I^{inst}, I^{SD}, respectively) along the diffraction vector s_{hkl}, plus the background (*Backg*):

$$I(s) = I^{inst}(s_{hkl}) \otimes I^{SD}(s_{hkl}) + Backg$$

The contribution of the generic family of reflection *hkl* to the specimen profile I^{SD} can be represented as a Fourier integral:

$$I_{hkl}(s_{hkl}) = \int_{-\infty}^{\infty} C_{hkl}(L) e^{2\pi i L \bullet s_{hkl}} dL$$

where s_{hkl} is the reciprocal space coordinate relative to the peak centroid of the hkl subcomponent and $C_{hkl}(L)$ is the product of the FT relative to each broadening source:

$$C_{hkl}(L) = A^{S}_{hkl}(L) \bullet A^{D}_{hkl}(L) \bullet A^{F}_{hkl}(L)$$

In this equation, $A^{S}_{hkl}(L)$ accounts for size effects (small dimension and shape of the coherently scattering domains), and the two other terms are the FT relative to line ($A^{D}_{hkl}(L)$) and planar ($A^{F}_{hkl}(L)$) defects.

The microstructural parameters refined during the fitting procedure are: m and σ, the parameters of the crystallite size distribution, ρ, the dislocation density, Re the effective outer cutoff radius of the dislocation field. These microstructural parameters are the common parameters which connect the different reflections during the simultaneous fitting. A lognormal distribution of spherical grains was considered.

Finally, faulting on (111) dense planes is described by two parameters, faulting probability α (deformation faults) and $\acute{o}$ (twin faults), according to Warren's theory and some recent modifications [43]. Concerning dislocations: the dislocation type corresponds to the {111}[110] primary slip system for fcc metals (Burgers vector modulus $|\mathbf{b}| = a\sqrt{3}/2$), for which the average contrast factor $\overline{C_{\{hkl\}}}$ was calculated using the elastic constants of pure gold [38]. Fig. 2 shows the experimental and modelled pattern of the AuNPs-GPE sample. The reliability factor R_{wp}, which is about 4 %, supports the excellent agreement between the experimental data and the refined model. The corresponding domain size distribution is shown in the *inset* of Fig. 2. Although both size and dislocation effects contribute to the observed line broadening, the size effect clearly dominates in this case. The microstrain effect, while small, is still measurable and provides a meaningful correction to the profile modeling. Specifically, an average dislocation density of 9.3×10^{16} m^{-2} was refined, indicating that the microstrain effect, though non-negligible, plays a secondary role compared to the prevailing size effect.

Summarily, the outcomes obtained by detailed XRPD analysis using WPPM, perfectly in line with other similar results reported by the existing literature in the field, highlighted the crystallite size and dislocation density, key factors that could influence the AuNPs-GPE behavior. Beyond size, defects within the crystal lattice introduce regions of altered electronic structure and local strain, which can modify

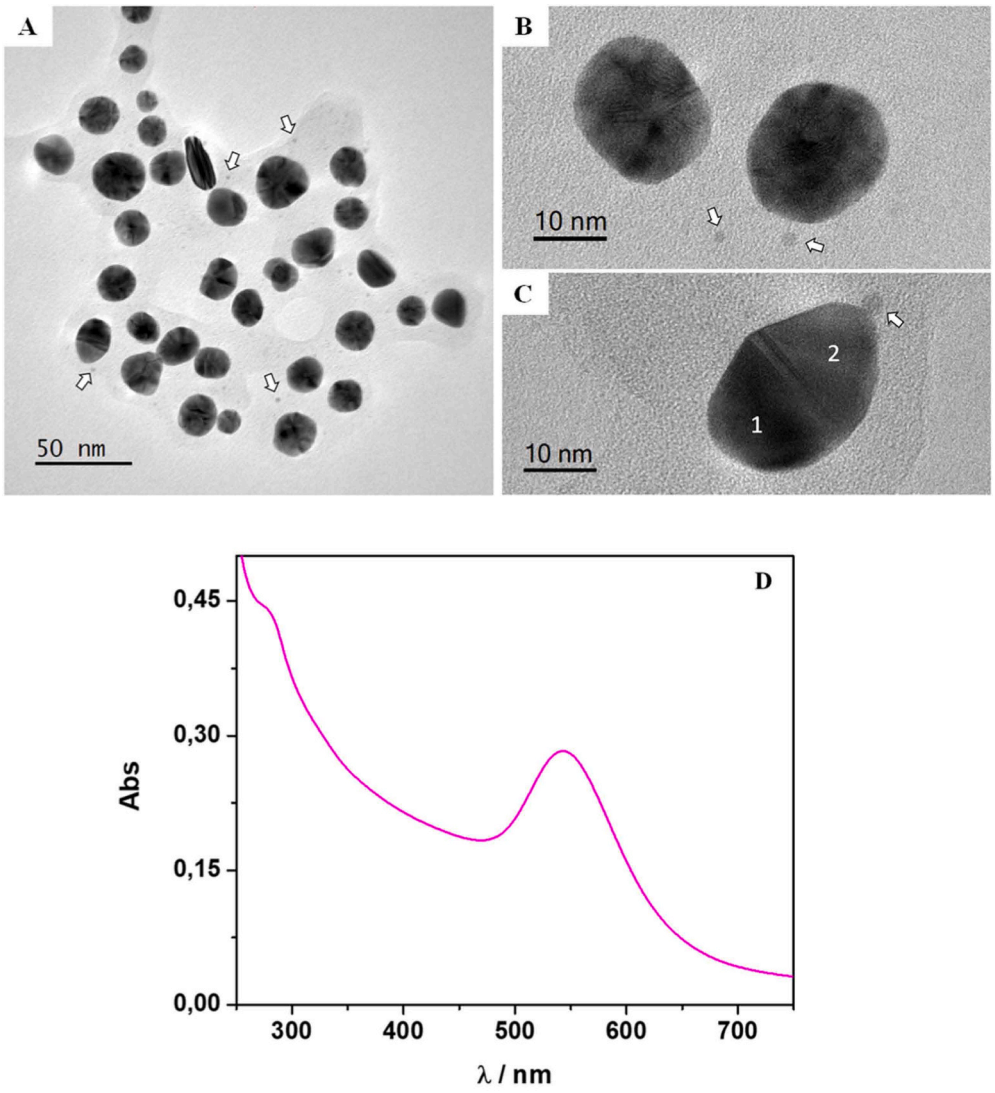

(caption on next page)

Fig. 1. TEM images (**A-C**) referred to the stock, non-diluted, AuNPs-GPE colloidal solution. In detail, panel **A** reports the BF-TEM image of AuNPs-GPE. The image is dominated by diffraction contrast: particles (or portions of a particle) that are close to Bragg conditions appear dark; those that are far away from Bragg conditions appear bright. The patchy dark/bright contrast within each particle suggests that each particle, actually, is a polycrystal with coherently scattering domains much smaller than the apparent dimension of the particle itself. High magnification image of two particles showing inhomogeneous contrast; the one at the upper left shows features consistent with cyclic twinning and Moiré fringes with different orientation, suggesting superposition of domains with different orientation (**B**). High magnification of a particle showing (at least) two distinct domains (1 and 2) separated by stacking faults, probably parallel twins. Arrows in all figures indicate very small (1–2 nm) particles (**C**). Panel **D** reports the UV-Visible spectrum of a dilution 1:5 from the stock AuNPs-GPE solution. Results of LeBail refinement for the AuNPs-GPE powder sample. The black and red profiles represent the observed and simulated data, respectively. (**E**).

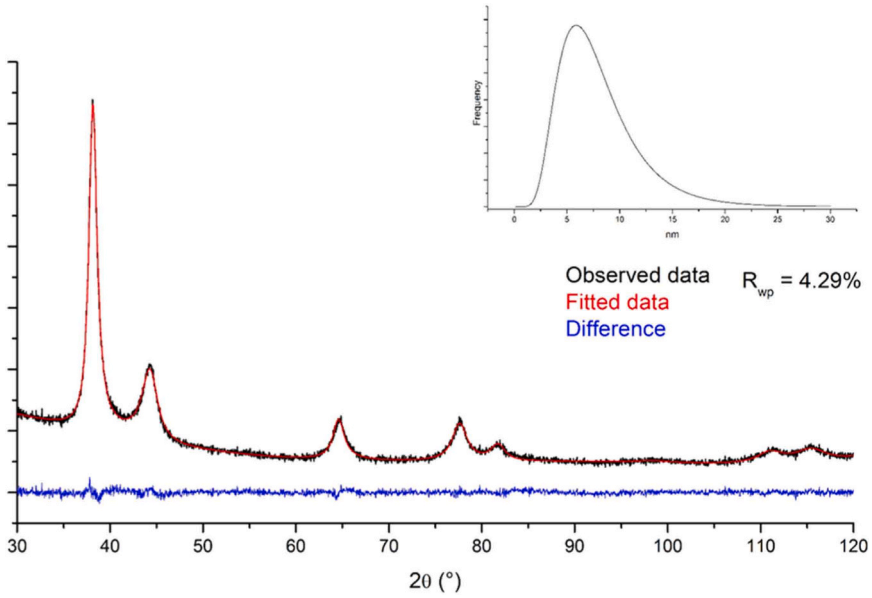

Fig. 2. XRPD pattern of AuNPs-GPE sample. The black line corresponds to raw data, and red profile to the WPPM result. The residual (difference between raw data and calculated curve) is also shown at the bottom of the pattern. The grain size distribution obtained by WPPM is represented by the histogram in the *inset*.

surface energy. These defects observed are strictly related to the nature of the polyphenolic pool which functionalized the AuNPs-GPE surface, since the crystalline domains arose during the synthetic process. Specifically, it can be assumed that the number of defects influences polyphenols' binding to allow other crystals' growth, and vice versa.

3.3. HPLC-MS/MS analyses

3.3.1. Evaluation of phenolic composition of AuNPs-GPE by HPLC-MS/MS analysis

The phenolic profile of AuNPs-GPE was characterized by HPLC-MS/MS using a validated MRM-based method (Table S1). The quantitative evaluation focused on a selection of representative polyphenols, identified from literature as the most characteristic and abundant compounds naturally present in grape pomace, in order to provide a meaningful overview of their incorporation efficiency into AuNPs-GPE. 20 phenolic compounds were investigated, and their presence onto the gold nanoparticles' surface was retrieved and reported in Table 1. A group of compounds, including catechin, epicatechin, gallic acid, quercetin, and phloretin showed high to complete occurrence ($\geq$ 90 %). These molecules typically possess multiple hydroxyl groups and/or planar aromatic systems, favoring both Au(III) ions reduction to Au(0), and stable surface capping through π–π interactions and metal chelation mechanisms [44]. Flavonoids such as hyperoside (73.2 %), kaempferol-3-*O*-glucoside (83.4 %), and flavanols as procyanidin A2 (70.8 %) also exhibited high presence, supporting the role of flavonol glycosides and proanthocyanidins as stabilizing agents in AuNPs' formation. Moreover, some polyphenols displayed low occurrence, such as chlorogenic acid (7.6 %), apigenin-7-*O*-glucoside (3.5 %), and phloridzin (39.9 %). These differences likely arise from structural features that reduce their ability to interact with the nanoparticles' surface. The comparison between aglycones and their glycosylated compounds revealed that glycosylation significantly reduces the occurrence degree. Moreover, the presence of sugar moieties increases molecular size and polarity, thereby reducing affinity for hydrophobic or metallic surfaces. For example, the aglycone quercetin was fully retrieved, while its glycosylated form, hyperoside, reached only 73.2 %. Similarly, phloridzin exhibited poor presence compared to the aglycone phloretin.

Table 1
Occurrence degree percentages of selected polyphenols in AuNPs-GPE determined by HPLC-MS/MS analysis.

Compound	Occurrence degree %
Catechin	100,00
Epicatechin	100,00
Procyanidin A2	70,75
Procyanidin B2	100,00
Quercetin	99,33
Chlorogenic Acid	7,56
Apigenin 7-*O*-glucoside	3,50
Naringin	60,42
Phloretin	94,83
Phloridzin	39,91
Rutin	53,38
Gallic acid	100,00
p-Coumaric acid	41,95
Quercetin 3-*O*-glucoside	93,49
Hyperoside	73,22
Kaempferol 3-*O*-glucoside	83,43
Syringic Acid	81,80
Malvidin 3-*O*-galactoside	93,80
Petunidin-3-*O*-glucoside	51,01
Malvidin 3-*O*-(*p*-coumaroyl) glucoside	96,86

3.3.2. Validation of the HPLC-MS/MS method for polyphenols analysis

The HPLC-MS/MS method for polyphenols analysis was rigorously validated according to ICH guidelines and showed excellent performance in terms of linearity, sensitivity, reproducibility, and absence of carry-over, as summarized in Table S2. Calibration curves for all target analytes were characterized by high coefficients of determination ($R^2 \geq 0.999$), confirming the linearity of response across the tested concentration ranges. Notably, the linear range was broad for all compounds, which supports the method's applicability for both trace and high-concentration quantification. This is particularly effective for complex matrices such as plant-derived nanoparticles, where analyte concentrations may vary significantly. The LODs and LOQs values were in the low ppb range for all compounds, indicating high method sensitivity. Analytical precision was evaluated through repeated injections of QC samples, and all compounds exhibited RSD% values < 5 %, highlighting high method reproducibility both in terms of peak area and retention time and supporting the reliability of the method. In addition, carry-over tests confirmed negligible residual signal (<0.1 %) for all polyphenols. Overall, the HPLC-MS/MS method demonstrated robust analytical performance and was suitable for the quantification of trace levels of polyphenols in the nanoparticles' colloidal solution, ensuring accurate monitoring of compound incorporation and permeation in the subsequent analyses.

3.3.3. Skin permeation of AuNPs-GPE and polyphenols

The *ex vivo* permeation profiles of AuNPs-GPE and selected polyphenols across porcine skin were evaluated using Franz diffusion cells at 4, 8, and 24 h, and the results are summarized in Fig. 3 and Table S3. If AuNPs-GPE were not accumulated in the skin, and completely retrieved in the receptor, on the other hand during their permeation, the release of polyphenols from AuNPs-GPE was retrieved. Interestingly, the investigation of the AuNPs skin penetration potential is a hot research topic that triggers considerable interest. Accordingly, it is a necessary step before proposing their application in biomedicine, since controversial issues arise when testing their behavior, raising potential risks for human health when interacting with physiological media and tissues [45,46]. In this study, the lack of AuNPs-GPE skin penetration evidence suggests that the proposed nanomaterials should be potentially not accumulated in tissues. Indeed, their accumulation can lead to toxicity through various mechanisms, including the generation of reactive oxygen species causing oxidative stress, DNA damage, and protein carbonylation [47]. Conversely, the results revealed distinct permeation behaviors among the quantified compounds, which appeared to be governed by a combination of their physicochemical properties and their presence onto the AuNPs-GPE surface. According to literature on transdermal drug delivery, physicochemical parameters such as molecular weight (MW < 600 Da), moderate lipophilicity (*XLogP* between 1 and 3), and low topological polar surface area (TopoPSA < 140–150 Å^2) are considered favorable for skin permeation [48,49]. However, in the context of our AuNPs-GPE system, these intrinsic properties alone do not fully explain the observed permeation profiles. Our data indicate that the occurrence degree onto the AuNPs strongly influences the release of each compound, which in turn impacts its availability for absorption across the skin. In particular, compounds that were tightly bound on the nanoparticle surface showed limited release and thus reduced transdermal permeation. On the other hand, low occurrence was generally associated with greater release from the gold-based colloidal solution, making the compound more available for skin diffusion. For example, catechin and gallic acid both exhibited 100 % occurrence into AuNPs and similar values of *XLogP* (0.14 and 0.7, respectively) and TopoPSA (110 and 98 Å^2), consistent with favorable permeation properties. As expected, they both showed comparable skin absorption values (38.5 % and 39.2 %, respectively), likely limited by their strong binding to the nanoparticle surface rather than by their molecular structure. Procyanidin B2 was present at nearly 100 % and showed a markedly lower absorption (17.9 %) compared to catechin and gallic acid. This value is probably due to the high TopoPSA (221 Å^2), which hinder passive diffusion across skin layers. Chlorogenic acid displayed the lowest presence in the AuNPs-GPE (7.56 %) but achieved the highest skin permeation (87.8 %). Its moderate MW (354.3 Da), relatively low *XLogP* (–0.4) and intermediate TopoPSA (165 Å^2) suggest high aqueous solubility and limited affinity for the hydrophobic AuNPs' surface, leading to rapid release and efficient diffusion. Finally, rutin showed intermediate presence (53.4 %), and moderate absorption (48.2 %), consistent with its very high MW (610.5 Da) and TopoPSA (266 Å^2). Although its *XLogP* (–1.3) and hydrophilicity limit interaction with the AuNPs-GPE surface, its large size and high polarity likely slowed its diffusion through the skin, explaining its intermediate behavior. These findings support the

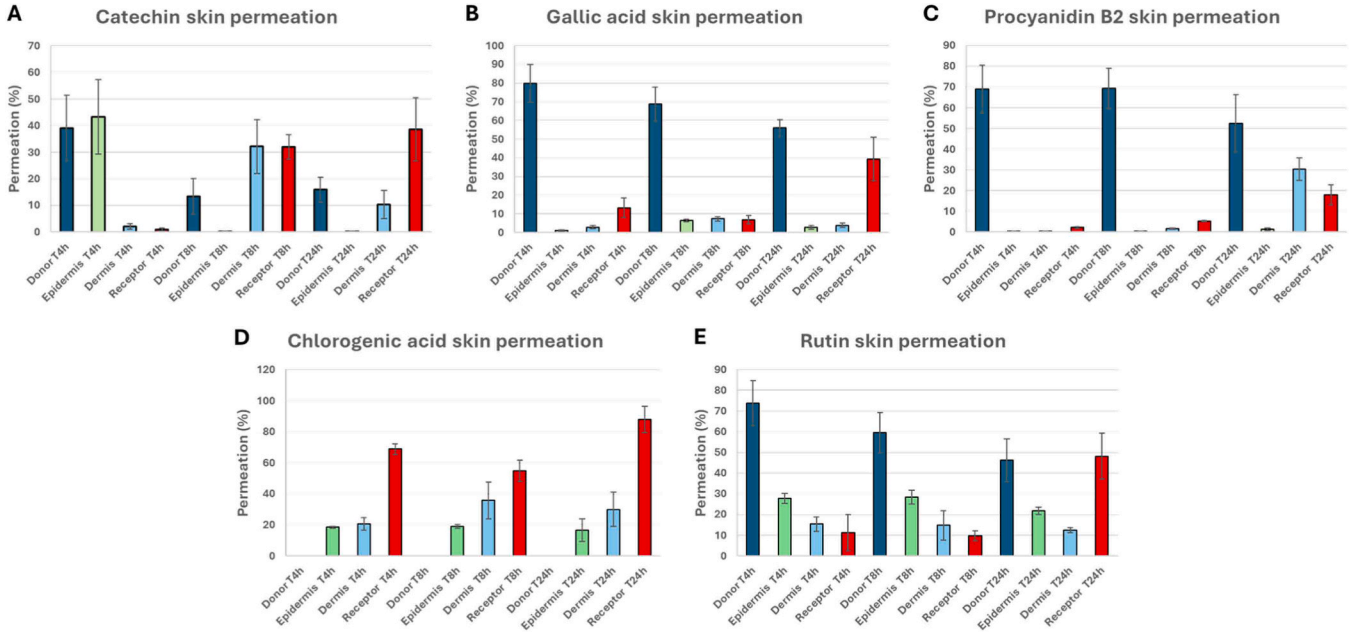

Fig. 3. Skin permeation profiles (% ± SD) of five representative polyphenols (catechin, gallic acid, procyanidin B2, chlorogenic acid, and rutin) (**A-E**) after 4, 8, and 24 h of incubation in Franz diffusion cells. Bar colors indicate the sampling compartment: donor (blue), epidermis (green), dermis (light blue), and receptor (red).

notion that skin absorption is jointly governed by molecular parameters and AuNPs-GPE-dependent release, with occurrence efficiency acting as a key modulator. Therefore, the data suggested that compounds which were partially or weakly bound to the AuNPs-GPE and possessed favorable intrinsic properties (small size, moderate polarity, and balanced lipophilicity) achieved optimal permeation in skin.

3.4. Proposing AuNPs-GPE in nanomedicine: biocompatibility and anti-inflammatory activity assessments

The AuNPs-GPE were tested on various cell lines, including human keratinocytes (HACAT) (Fig. 4), human fibroblasts (NHDF) (Fig. 5), human endothelial colony-forming cells (ECFC) (Fig. 6), and murine macrophages (RAW 264.7) (Fig. 7).

AuNPs-GPE were first administered to the cell types mentioned above with scalar dosages, from 1:40 of the stock solution to 1:10, to determine the best one in terms of non-cytotoxicity, instead allowing to appreciate the biological effect object of interest. Data reported in Figure S5 show that cell viability was not affected by any of the AuNPs-GPE concentrations tested, and thus the highest concentration (1:10) was selected for further experiments.

HACAT cells, which constitute the primary barrier-forming epithelium, were pre-treated overnight (O/N) with AuNPs-GPE to allow for nanoparticle internalization. Following treatment, the cells were evaluated 24 h after seeding for viability, using the MTT assay, and for functional capacity, using the wound healing assay. The MTT assay revealed that AuNPs-GPE treatment was neither cytotoxic nor exhibited any proliferative effect on HACAT cells. Similarly, the wound healing assay did not show significant differences or enhanced regenerative activity when compared to untreated control cells (Fig. 4).

Summarily, AuNPs-GPE did not alter keratinocytes' proliferation or migration, which suggests a favorable safety profile without inducing hyperproliferation or abnormal re-epithelialization. This lack of effect was consistent with a modulatory rather than stimulatory role at the epidermal level.

In contrast, NHDF, which are key regulators of extracellular matrix remodeling and wound contraction, exhibited modest enhancement in wound closure without increased proliferation, indicating functional modulation rather than mitogenic stimulation. Following the same experimental approach, AuNPs-GPE were also tested on the NHDF cell line. We did not observe any statistically significant variation in cell proliferation following the AuNPs-GPE treatment. However, the functional analysis performed using the wound healing assay revealed a modest increase in the regenerative capacity of AuNPs-pretreated cells

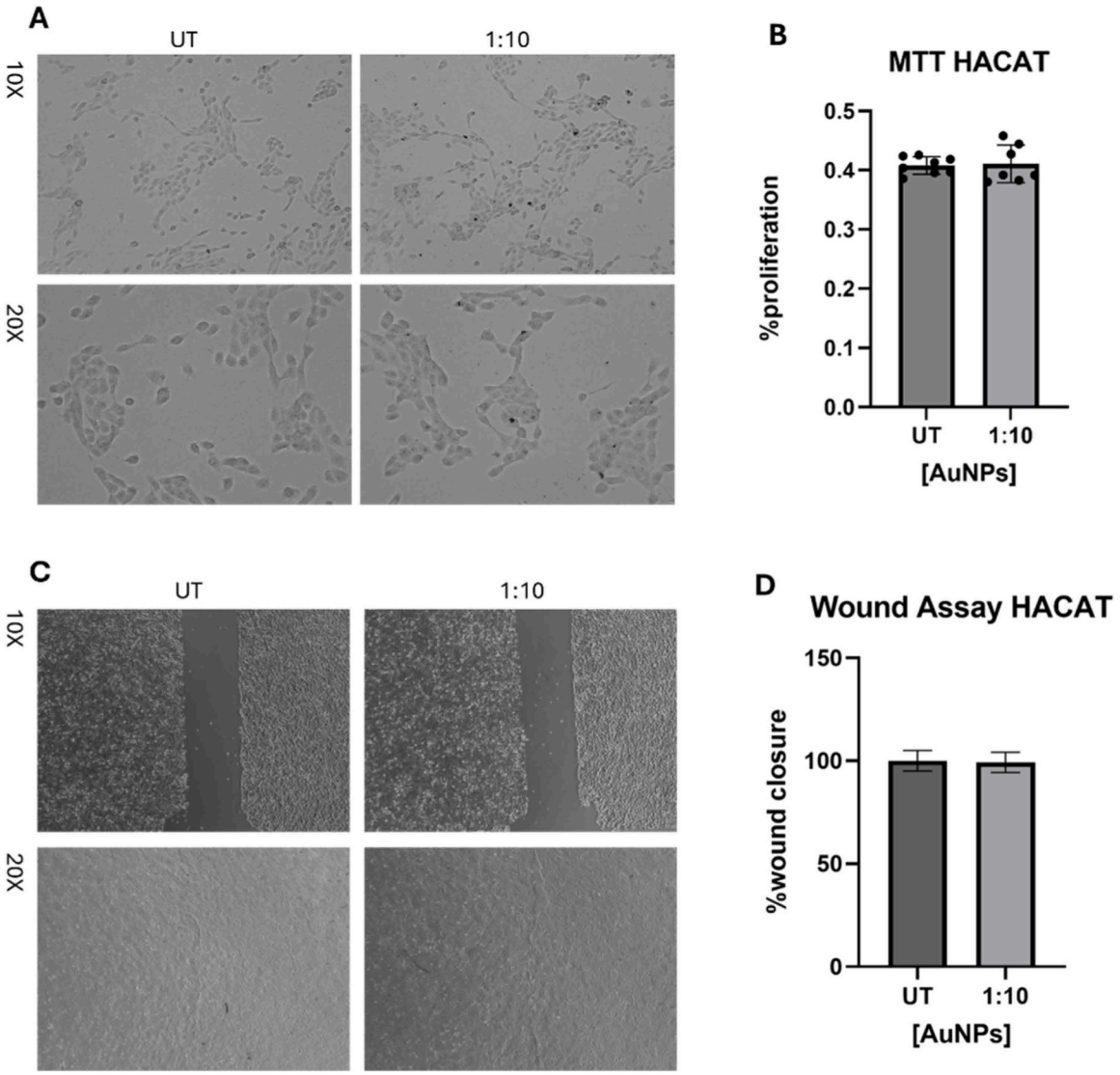

Fig. 4. Representative image of AuNPs-GPE internalization in HACAT cells (**A**). Viability assay of HACAT cells pre-treated with AuNPs-GPE and evaluated 24 h after seeding (**B**). Representative image (**C**) and quantitative analysis (**D**) of the regenerative capacity of AuNPs-pretreated HACAT cells.

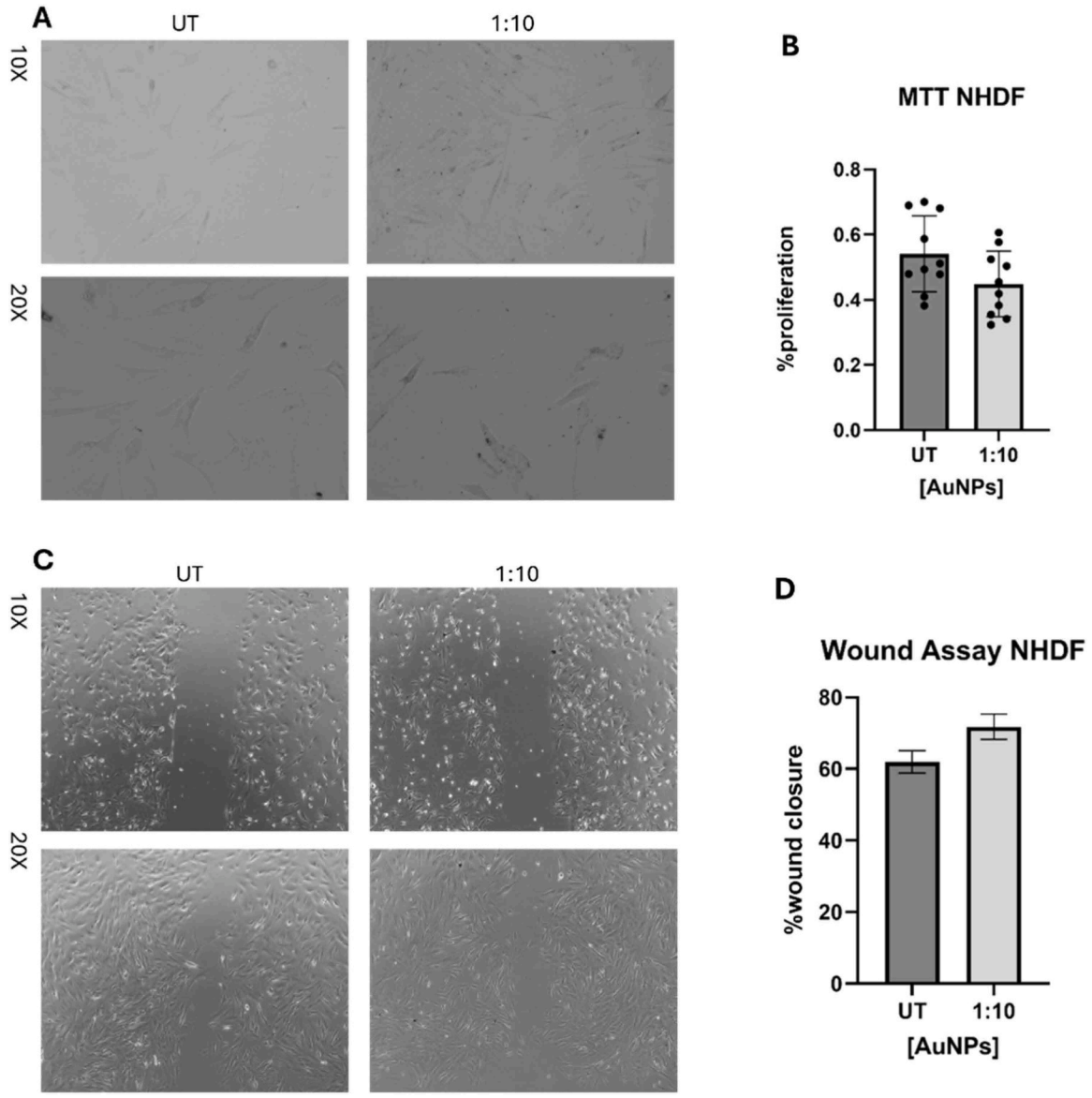

Fig. 5. Representative image of AuNPs-GPE internalization in NHDF cells (**A**). Viability assay of NHDF cells pre-treated with AuNPs-GPE and evaluated 24 h after seeding (**B**). Representative image (**C**) and quantitative analysis (**D**) of the regenerative capacity of AuNPs-pretreated NHDF cells.

compared to untreated controls (Fig. 5).

AuNPs-GPE were also tested on endothelial colony-forming cells (ECFC), which were treated overnight (O/N) to allow nanoparticle internalization. Specifically, cytotoxicity and the ability to induce morphogenesis were evaluated. Despite a slight, not statistically significant, decreased proliferation induced by AuNPs, the morphogenic assay, assessed 6 h after cell seeding, showed an enhanced morphogenic capacity in AuNPs-pretreated cells compared to untreated controls, as shown in the representative images and also the quantification charts of master junctions, length of master segments, meshes, length of segments, and nodes (Fig. 6**D**).

So, ECFC demonstrated enhanced angiogenic behavior, consistent with their high sensitivity to redox balance and polyphenol-mediated signaling, processes known to regulate endothelial migration and tubulogenesis.

The murine macrophage cell line RAW 264.7 was employed to evaluate any possible anti-inflammatory potential of AuNPs-GPE following activation induced by lipopolysaccharide (LPS) treatment [1 μg/mL]. Cells were first pre-treated overnight (O/N) with LPS to induce inflammatory activation, followed by a second overnight treatment with AuNPs-GPE. Cytotoxicity of the AuNPs was assessed both in the presence and absence of LPS, and, similarly to the previously tested cell lines, no cytotoxic effects were observed.

To investigate the anti-inflammatory activity of AuNPs-GPE, both qualitative and quantitative analyses of key pro-inflammatory signaling pathways were performed. Expression levels of TNF-α and IL-1β were measured by quantitative PCR (qPCR), while nuclear translocation of NFκB-p65 was assessed by immunofluorescence (IF). As shown in the representative images (Fig. 7**C**), a reduction in nuclear NFκB-p65 signal was observed in cells pre-treated with LPS and subsequently exposed to AuNPs-GPE, compared to the positive control treated with LPS alone. The qPCR data for IL-1β and TNFα (E) similarly show an increase in the expression of these markers with LPS treatment alone, and a reduction when cells are treated with LPS followed by AuNPs. This suggests decreased macrophage activation and supports a potential anti-inflammatory effect of AuNPs-GPE.

The outcomes were in line with the well-established ability of polyphenolic compounds to modulate macrophage polarization and inflammatory mediator production.

As a whole, these differential responses may arise from cell-

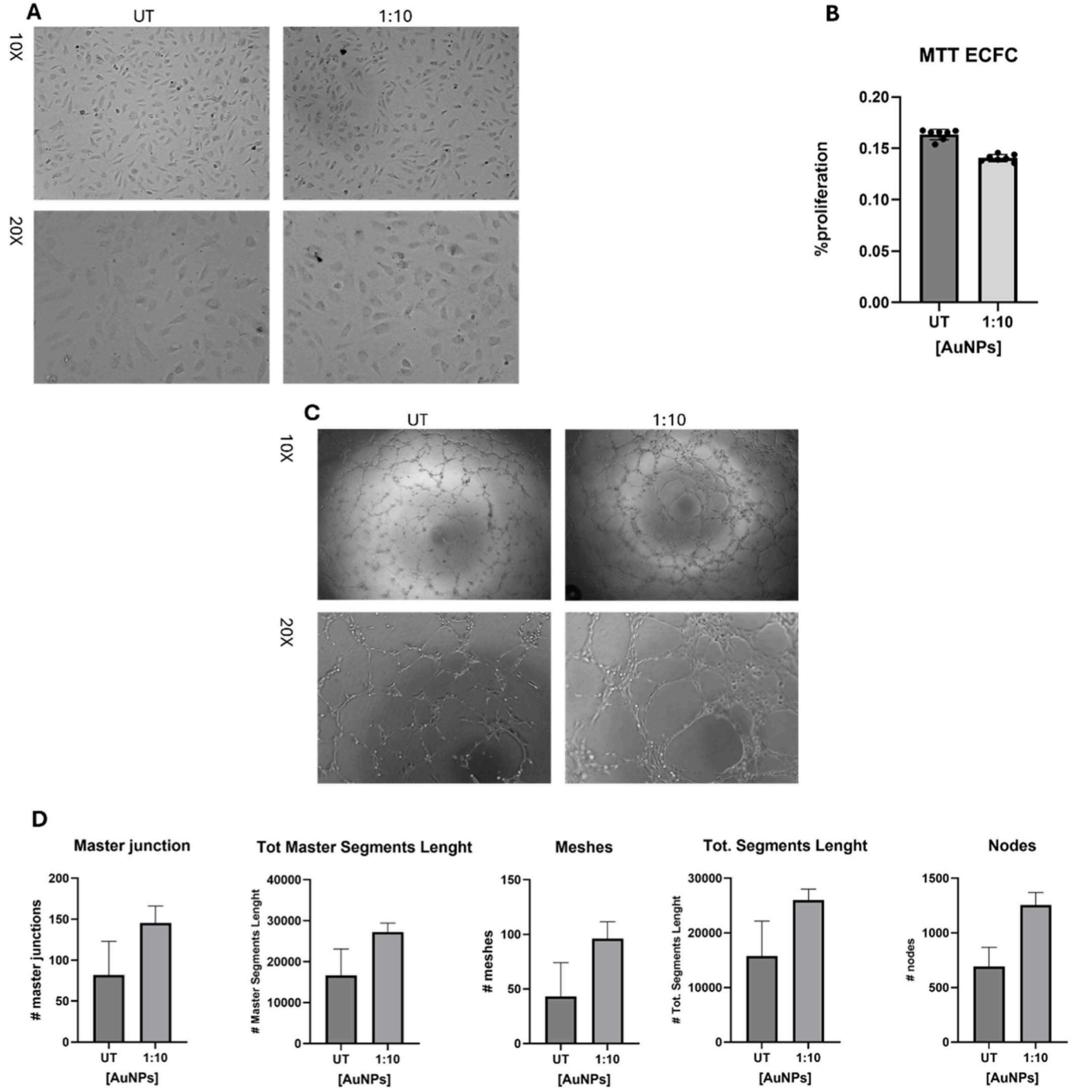

Fig. 6. Representative image of AuNPs-GPE internalization in ECFC cells (**A**). Viability assay of ECFC cells pre-treated with AuNPs-GPE and evaluated 24 h after seeding (**B**). Representative image (**C**) and quantitative analysis (**D**) of the morphogenic capacity of AuNPs pre-treated ECFC.

type–specific nanoparticle internalization rates, differential receptor expression, and distinct intracellular signaling networks. In addition, the polyphenolic components of the GPE likely acted pleiotropically, with different bioactive constituents preferentially influencing specific cellular pathways rather than eliciting uniform effects across all cell types. While the contribution of individual polyphenols or quantify uptake differences were not dissected in the present study, the polyphenolic pool that functionalizes AuNPs surface was the main responsible for the different effects observed.

To support this consideration, literature reports that polyphenols enhance wound healing by acting as redox-balance sensors, modulating inflammatory signaling, and extracellular matrix dynamics, enabling coordinated activity of immune cells, fibroblasts, keratinocytes, and endothelial cells across the phases of tissue repair [9–11,17].

4. Conclusions

Based on Green Chemistry and Circular Economy principles, an eco-friendly approach was followed for synthesizing AuNPs using a Grape Pomace water-based polyphenolic extract. An in-depth morphological, physical, and chemical investigation by means of XRPD, TEM, and HPLC-MS/MS analyses was performed on the AuNPs colloidal solution for unveiling that catechin, gallic acid, and quercetin were retrieved as the most abundant polyphenols constituting their decoration and

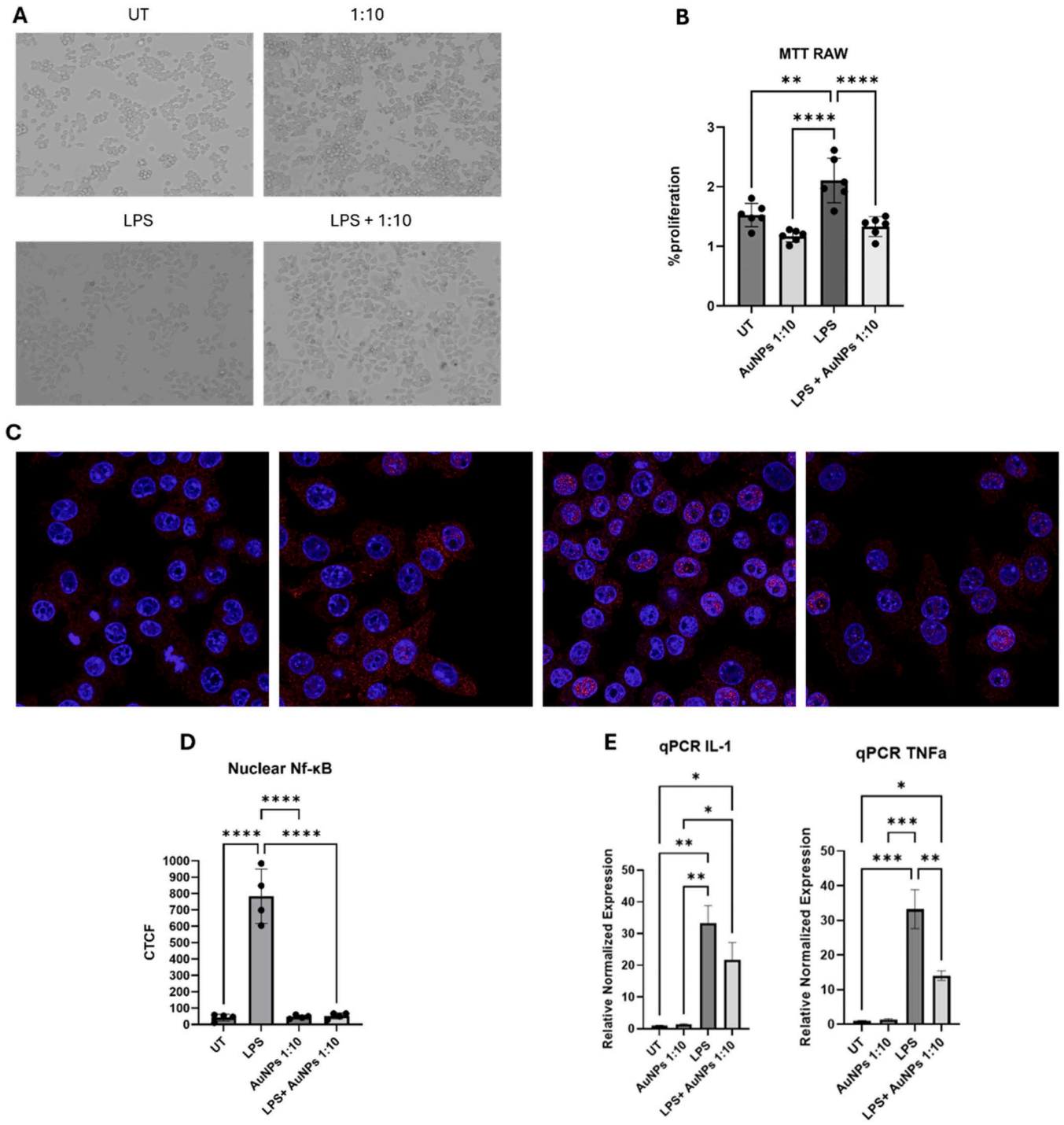

Fig. 7. Representative image of AuNPs-GPE internalization in RAW264.7 cells (**A**). Viability Assay of RAW 264.7 first pre-treated with LPS O/N followed by second O/N treatment with AuNPs (**B**). Representative image in IF of NfkB-p65 signal after treatment with LPS and AuNPs (**C**). Quantification of nuclear immunofluorescence signal using the JACoP plugin in ImageJ software (**D**). Gene expression analysis of IL-1β and TNF-α in RAW 264.7 cells evaluated by qPCR (**E**).

functionalization. Aiming to propose these AuNPs in regenerative medicine, a preliminary assessment of their transdermal potential through porcine skin was carried out using Franz diffusion vertical cells as models, showing a compound-dependent permeation profile. As a result, polyphenols tightly bound to the AuNPs surface exhibited moderate permeation, whereas chlorogenic acid, one of the poorly incorporated bioactive molecules, showed higher permeation rates, suggesting that both molecular features and incorporation efficiencies jointly affect skin absorption. The AuNPs' biocompatibility with HACAT, NHDF, and ECFC was further assessed performing the MTT assay, before investigating their role in accelerating wound healing and modulating the inflammatory response. First, it emerged that no cytotoxic or proliferative effects were observed on all cell lines when pretreated with AuNPs-GPE, that also exerted a modest increase in regenerative capacity on NHDF cell line. On the other hand, in the case of HACAT cell line, the wound healing assay did not show significant differences or enhanced regenerative activity if compared with untreated control. Additionally, AuNPs-GPE, since their morphogenic capacity, enhanced angiogenic processes in ECFC, helping vascular formation. Finally, for investigating the AuNPs-GPE anti-inflammatory

activity, murine macrophage cell line RAW 264.7 was employed, and key pro-inflammatory signalling pathways were studied by performing qualitative and quantitative analyses. For the purpose, TNF-α and IL-1β expression levels, and NFκB-p65 nuclear translocation were evaluated through qPCR and immunofluorescence, respectively. It was observed a reduction in nuclear NFκB-p65 signal in RAW 264.7 cells pre-treated with LPS and subsequently exposed to AuNPs, if compared with the positive control treated with LPS alone. Besides, also IL-1β and TNFα reduced their expression in the same conditions. The heterogeneous cellular responses observed in this study likely reflect the pleiotropic nature of polyphenolic-functionalized nanoparticles and the distinct biological roles of keratinocytes, fibroblasts, endothelial cells, and macrophages during different phases of wound healing. All these combined properties exhibited by the tested AuNPs-GPE suggest their promising application in tissue repair, giving the bases for next and more complex studies before proposing a real proof of concept as practical applications.

CRediT authorship contribution statement

Giancarlo Capitani: Software, Investigation, Data curation. **Vincenzo Piccolo:** Investigation, Data curation. **Anna Laurenzana:** Resources, Project administration, Data curation. **Elena Andreucci:** Resources, Investigation, Data curation. **Gennaro Ventruti:** Software, Investigation, Data curation. **Michela Pinto:** Writing – original draft, Investigation, Data curation. **Ritamaria Di Lorenzo:** Data curation. **Tenore Gian:** Data curation. **gubitosa jennifer:** Writing – review & editing, Visualization, Supervision, Resources, Project administration, Methodology, Investigation, Conceptualization. **Sonia Laneri:** Data curation. **Teresa Di Serio:** Investigation, Data curation. **Maria Maisto:** Data curation.

Declaration of Competing Interest

The authors declare that they have no known competing financial interests or personal relationships that could have appeared to influence the work reported in this paper.

Acknowledgements

This work has been supported by the following projects: “PRIN2022 con il finanziamento del Ministero dell’Università e della Ricerca nell’ambito del Bando relativo allo scorrimento delle graduatorie finali del bando PRIN 2022” entitled: “From wastes to gold nanoparticles: CHemistRY for Sustainable And Low environmental Impact bio-circular Strategies in cancer therapy (CHRY.S.A.L.I.S.)”; “MICS” (Made in Italy – Circular and Sustainable) Extended Partnership and received funding from the European Union Next-GenerationEU (PIANO NAZIONALE DI RIPRESA E RESILIENZA (PNRR)—MISSIONE 4 COMPONENTE 2, INVESTIMENTO 1.3—D.D. 1551.11–10–2022, PE00000004). The Authors would thank the winemaking farm “L’Archetipo”, Contrada Tafuri sp21, km7, Castellaneta, Taranto/Puglia 74011 (Italy) for having supplied the grape pomace.

Appendix A. Supporting information

Supplementary data associated with this article can be found in the online version at doi:10.1016/j.colsurfa.2026.139773.

Data availability

Data will be made available on request.

References

[1] F. Eker, E. Akdaşçi, H. Duman, M. Bechelany, S. Karav, Gold nanoparticles in nanomedicine: unique properties and therapeutic potential, Nanomaterials 14 (2024) 1854, https://doi.org/10.3390/nano14221854.
[2] L. Yao, D. Bojic, M. Liu, Applications and safety of gold nanoparticles as therapeutic devices in clinical trials, J. Pharm. Anal. 13 (2023) 960–967, https://doi.org/10.1016/j.jpha.2023.06.001.
[3] T.P. Patil, A.A. Vibhute, S.L. Patil, T.D. Dongale, A.P. Tiwari, Green synthesis of gold nanoparticles via Capsicum annum fruit extract: characterization, antiangiogenic, antioxidant and anti-inflammatory activities, Appl. Surf. Sci. Adv. 13 (2023) 100372, https://doi.org/10.1016/j.apsadv.2023.100372.
[4] W.C. Ko, S.J. Wang, C.Y. Hsiao, C.T. Hung, Y.J. Hsu, D.C. Chang, C.F. Hung, Pharmacological role of functionalized gold nanoparticles in disease applications, Molecules 27 (2022) 1551, https://doi.org/10.3390/molecules27051551.
[5] K. Koushki, P. Biswal, G.V. Vijay, M. Sadeghi, S. Dehnavi, N.T. Tra, S.K. Samala, M. Yousefi Taba, A.B. Vasan, E. Han, Y. Mackeyev, S. Krishnan, Immunomodulatory effects of gold nanoparticles: impacts on immune cells and mechanisms of action, Nanomaterials 15 (2025) 1201, https://doi.org/10.3390/nano15151201.
[6] Z. Deng, C. Yang, T. Xiang, C. Dou, D. Sun, Q. Dai, Z. Ling, J. Xu, F. Luo, Y. Chen, Gold nanoparticles exhibit anti-osteoarthritic effects via modulating interaction of the “microbiota-gut-joint” axis, J. Nanobiotechnol. 22 (2024) 157, https://doi.org/10.1186/s12951-024-02447-y.
[7] A. Chillà, C. Anceschi, F. Scavone, S. Martinelli, J. Ruzzolini, E. Frediani, F. Margheri, T. Tahir, G.C. Concas, M. Gisbert, M. Cremona, F. Freire, R.Q. Aucélio, T.Saint Pierre, A.L. Rossi, M. Severi, R. Traversi, D. Bani, D. Guasti, N. Daldosso, M. Del Rosso, G. Fibbi, C. SantAnna, T. Del Rosso, A. Laurenzana, Sparking angiogenesis by carbon monoxiderich gold nanoparticles obtained by pulsed laser driven CO_2 reduction reaction, J. Nanobiotechnol. 23 (2025) 590, https://doi.org/10.1186/s12951-025-03680-9.
[8] V.C. Thipe, A.R. Karikachery, P. Çakılkaya, U. Farooq, H.H. Genedy, N. Kaeokhamloed, D.-H. Phan, R. Rezwan, G. Tezcan, E. Roger, K.V. Katti, Green nanotechnology—An innovative pathway towards biocompatible and medically relevant gold nanoparticles, J. Drug Deliv. Sci. Technol. 70 (2022) 103256, https://doi.org/10.1016/j.jddst.2022.103256.
[9] J. Gubitosa, V. Rizzi, A. Lopedota, P. Fini, A. Laurenzana, G. Fibbi, F. Fanelli, A. Petrella, V. Laquintana, N. Denora, R. Comparelli, P. Cosma, One pot environmental friendly synthesis of gold nanoparticles using Punica granatum Juice: a novel antioxidant agent for future dermatological and cosmetic applications, J. Colloid Interface Sci. 521 (2018) 50–61, https://doi.org/10.1016/j.jcis.2018.02.069.
[10] J. Gubitosa, V. Rizzi, P. Fini, A. Laurenzana, G. Fibbi, C. Veiga-Villauriz, F. Fanelli, F. Fracassi, A. Onzo, G. Bianco, C. Gaeta, A. Guerrieri, P. Cosma, Biomolecules from snail mucus (Helix aspersa) conjugated gold nanoparticles, exhibiting potential wound healing and anti-inflammatory activity, Soft Matter 16 (2020) 10876–10888, https://doi.org/10.1039/D0SM01638A.
[11] J. Gubitosa, V. Rizzi, A. Laurenzana, F. Scavone, E. Frediani, G. Fibbi, F. Fanelli, T. Sibillano, C. Giannini, P. Fini, P. Cosma, The “End Life” of the grape pomace waste become the new beginning: the development of a virtuous cycle for the green synthesis of gold nanoparticles and removal of emerging contaminants from water, Antioxidants 11 (2022) 994, https://doi.org/10.3390/antiox11050994.
[12] J. Gubitosa, V. Rizzi, F. Maggi, A. Laurenzana, G. Caprioli, C. Anceschi, A. M. Mustafa, P. Fini, P. Cosma, From Kiwi Peels’ “End-of-Life” to gold nanoparticles: the upcycling of a waste, BioNanoScience 13 (2023) 1703–1725, https://doi.org/10.1007/s12668-023-01179-x.
[13] P.B. Santhosh, J. Genova, H. Chamati, Green synthesis of gold nanoparticles: an eco-friendly approach, Chemistry 4 (2022) 345–369, https://doi.org/10.3390/chemistry4020026.
[14] R.S. Varma, Greener approach to nanomaterials and their sustainable applications, Curr. Opin. Chem. Eng. 1 (2012) 123–128, https://doi.org/10.1016/j.coche.2011.12.002.
[15] P. Singh, Y.-J. Kim, D. Zhang, D.-C. Yang, Biological synthesis of nanoparticles from plants and microorganisms, Trends Biotechnol. 34 (2016) 588–599, https://doi.org/10.1016/j.tibtech.2016.02.006.
[16] I. Fatimah, Green synthesis of silver nanoparticles using extract of Parkia speciosa Hassk pods assisted by microwave irradiation, J. Adv. Res. 7 (2016) 961–969, https://doi.org/10.1016/j.jare.2016.10.002.
[17] V. De Matteis, M. Cascione, P. Pellegrino, R. Di Corato, M. Catalano, A. Miraglia, A. Scarano, A. Santino, M. Chieppa, R. Rinaldi, Multishaped bio-gold polyphenols bearing nanoparticles to promote inflammatory suppression, Nano Today 57 (2024) 102329, https://doi.org/10.1016/j.nantod.2024.102329.
[18] A.O.E. Eltahir, K.L. Lategan, O.M. David, E.J. Pool, R.C. Luckay, A.A. Hussein, Green synthesis of gold nanoparticles using liquiritin and other phenolics from glycyrrhiza glabra and their anti-inflammatory activity, J. Funct. Biomater. 15 (2024) 95, https://doi.org/10.3390/jfb15040095.
[19] J. Gubitosa, V. Rizzi, C. Marasciulo, F. Maggi, G. Caprioli, A.M. Mustafa, P. Fini, N. De Vietro, A.M. Aresta, P. Cosma, Realizing eco-friendly water-resistant sodium-alginate-based films blended with a polyphenolic aqueous extract from grape pomace waste for potential food packaging applications, Int. J. Mol. Sci. 24 (2023) 11462, https://doi.org/10.3390/ijms241411462.

[20] K. Singpanna, C. Pornpitchanarong, P. Patrojanasophon, T. Rojanarata, T. Ngawhirunpat, S.K. Li, P. Opanasopit, Chitosan capped-gold nanoparticles as skin penetration enhancer for small molecules: a study in porcine skin, Int. J. Pharm. 640 (2023) 123034, https://doi.org/10.1016/j.ijpharm.2023.123034.
[21] B. Palosz, E. Grzanka, S. Gierlotka, S. Stel'makh, R. Pielaszek, W. Lojkowski, U. Bismayer, J. Neuefeind, H.-P. Weber, W. Palosz, Application of X-ray powder diffraction to nano-materials - determination of the atomic structure of nanocrystals with relaxed and strained surfaces, Phase Transit 76 (2003) 171–185, https://doi.org/10.1080/0141159031000076129.
[22] P. Scardi, M. Leoni, R. Delhez, Line broadening analysis using integral breadth methods: a critical review, J. Appl. Crystallogr 37 (2004) 381–390, https://doi.org/10.1107/S0021889804004583.
[23] G. Sonavane, K. Tomoda, A. Sano, H. Ohshima, H. Terada, K. Makino, In vitro permeation of gold nanoparticles through rat skin and rat intestine: effect of particle size, Colloids Surf. B Biointerfaces 65 (2008) 1–10, https://doi.org/10.1016/j.colsurfb.2008.02.013.
[24] F. Larese Filon, M. Crosera, G. Adami, M. Bovenzi, F. Rossi, G. Maina, Human skin penetration of gold nanoparticles through intact and damaged skin, Nanotoxicology 5 (2011) 493–501, https://doi.org/10.3109/17435390.2010.551428.
[25] J. Bergmann, P. Friedel, R. Kleeberg, BGMN – a new fundamental parameter-based Rietveld program for laboratory X-ray sources, its use in quantitative analysis and structure investigations, Comm. Powder Diffr. Newsl. 20 (1998) 5–8.
[26] P. Scardi, M. Leoni, Y.H. Dong, Whole diffraction pattern-fitting of polycrystalline fcc materials based on microstructure, Eur. Phys. J. B. 18 (2000) 23–30, https://doi.org/10.1007/s100510070073.
[27] M. Leoni, R. Di Maggio, S. Polizzi, P. Scardi, X-raY Diffraction Methodology for the Microstructural Analysis of Nanocrystalline Powders: Application to Cerium Oxide, J. Am. Ceram. Soc. 87 (2004) 1133–1140, https://doi.org/10.1111/j.1551-2916.2004.01133.x.
[28] V. Campani, L. Scotti, T. Silvestri, M. Biondi, G. De Rosa, Skin permeation and thermodynamic features of curcumin-loaded liposomes, J. Mater. Sci. Mater. Med. 31 (2020) 18, https://doi.org/10.1007/s10856-019-6351-6.
[29] R. Di Lorenzo, I. Neri, G. Russo, S. Laneri, L. Grumetto, Tracking down of a selected panel of parabens: a validated method to evaluate their occurrence in skin layers, Cosmetics 9 (2022) 102, https://doi.org/10.3390/cosmetics9050102.
[30] C. Padula, A. Pappani, P. Santi, In vitro permeation of levothyroxine across the skin, Int. J. Pharm. 349 (2008) 161–165, https://doi.org/10.1016/j.ijpharm.2007.08.004.
[31] I. Neri, S. Laneri, R. Di Lorenzo, I. Dini, G. Russo, L. Grumetto, Parabens permeation through biological membranes: a comparative study using franz cell diffusion system and biomimetic liquid chromatography, Molecules 27 (2022) 4263, https://doi.org/10.3390/molecules27134263.
[32] R. Di Lorenzo, A. Bernardi, L. Grumetto, A. Sacchi, C. Avagliano, S. Coppola, A. F. de Giovanni di Santa Severina, C. Bruno, L. Paparo, S. Laneri, I. Dini, Phenylalanine Butyramide Is a New Cosmetic Ingredient with Soothing and Anti-Reddening Potential, Molecules 26 (2021) 6611, https://doi.org/10.3390/molecules26216611.
[33] Z.E. Jiménez Pérez, R. Mathiyalagan, J. Markus, Y.J. Kim, H.M. Kang, R. Abbai, K. H. Seo, D. Wang, V. Soshnikova, D.C. Yang, Ginseng-berry-mediated gold and silver nanoparticle synthesis and evaluation of their in vitro antioxidant, antimicrobial, and cytotoxicity effects on human dermal fibroblast and murine melanoma skin cell lines, Int. J. Nanomed. 12 (2017) 709–723, https://doi.org/10.2147/IJN.S118373.
[34] H.P. Borase, C.D. Patil, R.B. Salunkhe, R.K. Suryawanshi, B.K. Salunke, S.V. Patil, Phytolatex synthesized gold nanoparticles as novel agent to enhance sun protection factor of commercial sunscreens, Int. J. Cosmet. Sci. 36 (2014) 571–578, https://doi.org/10.1111/ics.12158.
[35] M. Arif, H. Raza, T. Akhter, UV-Vis spectroscopy in the characterization and applications of smart microgels and metal nanoparticle-decorated smart microgels: a critical review, RSC Adv. 14 (2024) 38120–38134, https://doi.org/10.1039/d4ra07643e.
[36] H.P. Klug, L.E. Alexander, X-ray diffraction procedures, 2nd ed, N. Y. John Wiley Sons (1974) 618–708, https://doi.org/10.1002/bbpc.19750790622.
[37] P. Scherrer, Bestimmung der inneren Struktur und der Größe von Kolloidteilchen mittels Röntgenstrahlen. In: Kolloidchemie, Springer, Berlin, 1918, pp. 98–100, https://doi.org/10.1007/978-3-662-33915-2_7.
[38] G.K. Williamson, W.H. Hall, X-Ray line broadening from filed aluminium and wolfram, Acta Met. 1 (1953) 22–31, https://doi.org/10.1016/0001-6160(53)90006-6.
[39] E. Prince, J.K. Stalick, Accuracy in powder diffraction II, 846, NIST Spec Publ No, Gaithersburg, MD: NIST, 1992.
[40] J.I. Langford, A.J.C. Wilson, Seherrer after sixty years: a survey and some new results in the determination of crystallite size, J. Appl. Crystallogr 11 (1978) 102–113, https://doi.org/10.1107/S0021889878012844.
[41] J.I. Langford, D. Louër, P. Scardi, Effect of a crystallite size distribution on X-ray diffraction line profiles and whole-powder-pattern fitting, J. Appl. Crystallogr 33 (2000) 964–974, https://doi.org/10.1107/S002188980000460X.
[42] A.C. Murrieta, D. Cavazos-Cavazos, P. Santos-Aguilar, J.L. Cholula-Díaz, F. F. Contreras-Torres, Microstructure of polycrystalline gold nanoparticles and thin-films from a comparative X-ray line profile analysis, Mater. Chem. Phys. 258 (2021) 123976, https://doi.org/10.1016/j.matchemphys.
[43] B.E. Warren, X-ray studies of deformed metals, Prog. Met. Phys. 8 (1959) 147–202, https://doi.org/10.1016/0502-8205(59)90015-2.
[44] T. Ahmad, M.A. Bustam, M. Irfan, M. Moniruzzaman, H.M.A. Asghar, S. Bhattacharjee, Mechanistic investigation of phytochemicals involved in green synthesis of gold nanoparticles using aqueous Elaeis guineensis leaves extract: Role of phenolic compounds and flavonoids, Biotechnol. Appl. Biochem 66 (2019) 698–708, https://doi.org/10.1002/bab.1787.
[45] H.I. Labouta, L.K. El-Khordagui, T. Kraus, M. Schneider, Mechanism and determinants of nanoparticle penetration through human skin, Nanoscale 3 (2011) 4989–4999, https://doi.org/10.1039/c1nr11109d.
[46] F. Larese Filon, M. Mauro, G. Adami, M. Bovenzi, M. Crosera, Nanoparticles skin absorption: New aspects for a safety profile evaluation, Regul. Toxicol. Pharm. 72 (2015) 310–322, https://doi.org/10.1016/j.yrtph.2015.05.005.
[47] C. Lopez-Chaves, J. Soto-Alvaredo, M. Montes-Bayon, J. Bettmer, J. Llopis, C. Sanchez-Gonzalez, Gold nanoparticles: distribution, bioaccumulation and toxicity. *In vitro* and *in vivo* studies, Nanomedicine 14 (2018) 1–12, https://doi.org/10.1016/j.nano.2017.08.011.
[48] D. Ramadon, M.T.C. McCrudden, A.J. Courtenay, R.F. Donnelly, Enhancement strategies for transdermal drug delivery systems: current trends and applications, Drug. Deliv. Transl. Res. 12 (2022) 758–791, https://doi.org/10.1007/s13346-021-00909-6.
[49] R.M. Abdallah, H.E. Hasan, A. Hammad, Predictive modeling of skin permeability for molecules: Investigating FDA-approved drug permeability with various AI algorithms, PLoS Digit Health 3 (2024) e0000483, https://doi.org/10.1371/journal.pdig.0000483.